Materials Science & Engineering A 941 (2025) 148607

Contents lists available at ScienceDirect

Materials Science & Engineering A

journal homepage: www.elsevier.com/locate/msea

# Influence of $B_4C$ alloying on the phase stability of Fe-Mn-Co-Cr-Si high entropy alloys fabricated using laser powder bed fusion

I.A.B. Moura [a,b,c,*], G.G. Ribamar [d,e], P. Agrawal [b], A. Roy [b], J. Shen [d], P. Freitas Rodrigues [c], E. Maawad [f], N. Schell [f], A.B. Pereira [e], J.P. Oliveira [d], R.S. Mishra [b,g]

[a] UNIDEMI, Department of Mechanical Engineering, NOVA School of Science and Technology, Universidade NOVA de Lisboa, Caparica, 2829-516, Portugal
[b] Center for Friction Stir Processing, Department of Materials Science and Engineering, University of North Texas, Denton, TX, 76203, USA
[c] CEMMPRE, ARISE, Department of Mechanical Engineering, University of Coimbra, Coimbra, 3030-788, Portugal
[d] CENIMAT/I3N, Department of Materials Science, NOVA School of Science and Technology, Universidade NOVA de Lisboa, Caparica, 2829-516, Portugal
[e] TEMA—Centre for Mechanical Technology and Automation, Department of Mechanical Engineering, Campus de Santiago, University of Aveiro, 3810-193, Aveiro, Portugal
[f] Institute of Materials Physics, Helmholtz-Zentrum Hereon, Max-Planck-Str. 1, Geesthacht, D-21502, Germany
[g] Advanced Materials and Manufacturing Processes Institute, University of North Texas, Denton, TX, 76207, USA

A R T I C L E I N F O

*Keywords:*
X-ray synchrotron radiation
Martensitic phase transformation
Phase stability
High entropy alloys

A B S T R A C T

This study investigates the impact of 0.25 wt% $B_4C$ addition on the microstructure, phase stability, and mechanical properties of metastable $Fe_{40}Mn_{20}Co_{20}Cr_{15}Si_5$ (at.%) high-entropy alloys (HEAs) fabricated via laser powder bed fusion (LPBF). A comparative analysis between $B_4C$-containing (BC) and $B_4C$-free (CS) alloys explored the influence of varying LPBF parameters. Electron backscattered diffraction (EBSD) revealed a strong dependence of microstructure on laser power and scanning speed in CS alloys, with significant variations in grain size and morphology. Conversely, BC alloys exhibited enhanced microstructural stability, indicating a more robust grain growth mechanism due to the influence of $B_4C$. $B_4C$ addition also promoted grain refinement and stabilized the γ-f.c.c. phase. Mechanical testing showed a substantial increase in yield strength (YS) from 508 MPa (CS) to 670 MPa (BC) and a moderate increase in ultimate tensile strength (UTS) from 843 MPa (CS) to 854 MPa (BC). However, ductility decreased from 25 % to 5 %. Critically, synchrotron X-ray diffraction revealed deviations from the ideal c/a ratio (1.633) for both alloys. CS alloys showed an increase in c/a ratio after tensile deformation, indicative of a deformation-induced phase transformation, while BC alloys exhibited a decrease, suggesting a distinct deformation mechanism. This novel observation provides key insights into the role of $B_4C$ in controlling the deformation behavior of this HEA.

## 1. Introduction

Metastable high-entropy alloys (HEAs) represent a significant advancement in material science, addressing the longstanding challenge of balancing strength and ductility in alloys [1–3]. By combining the solid solution strengthening of HEAs with advanced material hardening mechanisms, these alloys overcome the conventional trade-offs imposed by traditional metallurgical methods [3]. Their innovative design leverages a dual-phase microstructure, where the reduced thermal stability of the high-temperature phase promotes interface hardening, and the mechanical instability of the low-temperature phase triggers transformation-induced hardening. This synergistic interplay results in superior mechanical properties, making metastable HEAs a promising solution for energy-efficient and lightweight applications [3,4].

The study of metastable HEAs offers a valuable framework for exploring the influence of γ-f.c.c.→ε-h.c.p. phase transformations on mechanical performance, particularly concerning volumetric changes during deformation [5,6]. Structural changes, such as variations in the c/a ratio, provide critical insights into the interplay between phase stability and mechanical behavior in HEAs [7]. The development of transformation-induced plasticity-assisted dual-phase high-entropy alloys (TRIP-DP-HEAs) exemplifies the potential of metastability engineering in these materials. Unlike many conventional structural materials, TRIP-DP-HEAs exhibit an exceptional balance of strength and

---

* Corresponding author. UNIDEMI, Department of Mechanical Engineering, NOVA School of Science and Technology, Universidade NOVA de Lisboa, Caparica, 2829-516, Portugal.

*E-mail addresses:* ia.moura@campus.fct.unl.pt (I.A.B. Moura), jp.oliveira@fct.unl.pt (J.P. Oliveira).

https://doi.org/10.1016/j.msea.2025.148607
Received 27 February 2025; Received in revised form 25 April 2025; Accepted 29 May 2025

ductility [5,6]. This improved ductility arises from an enhanced strain-hardening capacity, driven by the combined effects of dislocation-induced hardening in the stable phase and transformation-induced hardening in the metastable phase [5,6].

Laser powder bed fusion (LPBF) has emerged as a transformative method for fabricating HEAs, enabling the creation of complex, high-performance materials with tailored properties [5,6,8]. The effectiveness of LPBF lies in its ability to refine and control microstructures through precise adjustments of parameters such as laser power, scanning speed, and layer thickness [9]. These controlled microstructures are particularly critical for HEAs designed for extreme environments. However, despite significant progress, challenges remain in achieving reliable microstructural control, maintaining phase stability, and fully understanding deformation mechanisms, such as the TRIP effect [10,11]. Recent studies highlight that adjusting laser power and scanning speed can effectively regulate cooling rates, significantly impacting the formation of either single-phase or multi-phase structures in HEAs [8,9]. This relationship between process parameters underscores the importance of a detailed understanding of additive manufacturing (AM) techniques to unlock the full potential of HEAs in high-performance applications. Current research efforts are focused on developing predictive models and advanced in-situ monitoring tools to optimize the AM process and ensure consistent quality in fabricated components [10,11].

Regarding alloying with ceramic particles, literature has shown that incorporating boron carbide ($B_4C$) into alloys introduces additional complexity and opportunities for tailoring material properties [12–14]. $B_4C$, renowned for its high hardness and thermal stability, is commonly employed as a reinforcing phase or grain refiner [12–14]. In HEAs, its inclusion can influence phase stability and mechanical behavior depending on factors such as alloy composition and cooling rate. Additionally, boron and carbon exhibit a strong tendency to segregate at grain boundaries, particularly in Fe-based systems, enhancing alloy strength through mechanisms such as solid solution strengthening and grain boundary strengthening [15–21].

In this study, we investigate the mechanisms underlying phase transformations and mechanical behavior in metastable HEAs, analyzing how the presence of $B_4C$ affects phase transformations, variations in the c/a ratio of ε-h.c.p. phase, and overall phase stability due to deformation. By contrasting these mechanisms, we aim to deepen the understanding of metastable HEA behavior and identify pathways to optimize their microstructural and mechanical performance for advanced applications.

## 2. Materials and methods

### 2.1. Experimental materials and LPBF process

Two groups of pre-alloyed HEAs were studied. The first group, with composition $Fe_{40}Mn_{20}Co_{20}Cr_{15}Si_5$ (at.%), referred to as CS, was gas atomized at Oerlikon Metco. The powders presented $D_{10}$ value of ≈15 μm and $D_{100}$ value of ≈45 μm, while the powder distribution and morphology are displayed in Fig. S1 in the Supplementary Material. CS powder was LPBF printed using TRUMPF (Truprint 1000 machine) with a maximum 200 W laser with a spot size of 55 μm. An inert argon atmosphere with oxygen content ≤100 ppm (0.01 wt%) was used. A scan rotation of 67° was used between alternating layers. The printed rectangular blocks were built with dimensions of 10 × 22 × 22 mm in height, width, and thickness, respectively. The nominal and measured chemical composition via EDS (energy dispersive X-ray spectroscopy) of the powder is shown in Table 1. The printing parameters used, namely laser power (P), scanning speed (V), hatching space (h), layer thickness (l), and volumetric energy density (VED, $J/mm^3$), as well as sample nomenclature for CS conditions used in this work, are shown in Table 2. The VED was calculated using Equation (1).

**Table 1**
Nominal and experimental chemical composition of gas atomized powder in at. %.

| Elements | Fe | Mn | Co | Cr | Si |
|---|---|---|---|---|---|
| Nominal | 40.0 | 20.0 | 20.0 | 15.0 | 5.0 |
| Experimental | 41.8 | 18.8 | 19.1 | 14.8 | 5.5 |

$$VED = P/Vhl \qquad (1)$$

To directly assess the impact of $B_4C$ addition on the properties of the CS alloy, 0.25 wt% $B_4C$ powder (average particle size of ≈5 μm) was added to the CS powders. The combined powder was mixed with high-speed rolling for 24 h to ensure uniform distribution to produce the second alloy used in this study. These samples with $B_4C$ addition were labeled as BC. To assess the influence of $B_4C$ under controlled laser processing conditions, the four initial parameter sets used for CS samples were applied to BC alloys. This ensured a direct comparison of the $B_4C$ effect on microstructural and mechanical properties while keeping other variables unchanged. The parameters used for BC conditions are shown in Table 2. The experimental design was refined based on preliminary findings. The BC printed blocks were built with dimensions of 18 × 20 × 15 mm in height, width, and thickness, respectively.

### 2.2. Microstructural characterization

The samples were machined using an electro-discharge machine (EDM) from the plane parallel to the building direction. Machined samples were then polished metallographically to a 0.02 μm surface finish using SiC paper, followed by polishing using diamond paste and, finally, a colloidal silica solution. Optical micrographs of the specimens were taken using a Nikon Eclipse ME600 optical microscope in polished samples to observe defects such as pores. Electron backscattered diffraction (EBSD) measurements were performed using a FEI Nova nano SEM equipped with a Hikari detector, operating at 20 kV and 6.1 nA current, using a 70° pre-tilt holder. EBSD data was processed using the orientation imaging microscopy (OIM) software and the open-source Mtex software [22].

Prior γ-f.c.c. orientation was calculated to better compare grain size and morphology for samples that presented a considerable amount of ε-h.c.p. in the EBSD measurements. Shoji-Nishiyama (S-N) orientation relationship (OR) was used to reconstruct the parent γ-f.c.c. orientation phase. Non-indexed and low-quality EBSD points were not used on the representations nor the prior γ-f.c.c. calculations, being represented as white points in the EBSD maps.

### 2.3. Tensile testing

A miniature tensile testing machine was used for mechanical characterization. For each condition, three tensile specimens with a gauge length of 5 mm and width of 1.25 mm were machined with EDM, where the gauge length was maintained along the building direction, as presented in Fig. 1. The mini tensile specimens were polished to a surface finish of 1 μm, and the tensile tests were carried out at room temperature at a strain rate of $10^{-3}$ $s^{-1}$. The calculated yield strength, elongation, and ultimate tensile strength for each condition are an average of three tests.

### 2.4. Synchrotron X-Ray diffraction (SXRD)

SXRD line scan was used to investigate microstructure evolution after mechanical testing on the samples with different processing parameters. The SXRD was performed at the P07 High Energy Materials Science (HEMS) beamline [23] at PETRA III/DESY, which is partially operated by the Helmholtz-Zentrum Hereon. An incident monochromatic X-ray beam of 500 × 100 μm, with an energy of 87.1 keV

**Table 2**
LPBF process parameters and samples nomenclature used in the present work.

| Nomenclature | | Power (P, W) | Scanning speed (V, mm/s) | Hatching space (h, mm) | Layer thickness (l, mm) | Volumetric energy density (VED, J/mm$^3$) |
|---|---|---|---|---|---|---|
| Without $B_4C$ | With $B_4C$ | | | | | |
| **CS 1** | **BC 1** | 150 | 800 | 0.1 | 0.04 | 46.9 |
| **CS 2** | **BC 2** | 150 | 600 | 0.1 | 0.04 | 62.5 |
| **CS 3** | **BC 3** | 160 | 800 | 0.1 | 0.04 | 50.0 |
| **CS 4** | **BC 4** | 180 | 800 | 0.1 | 0.04 | 56.3 |

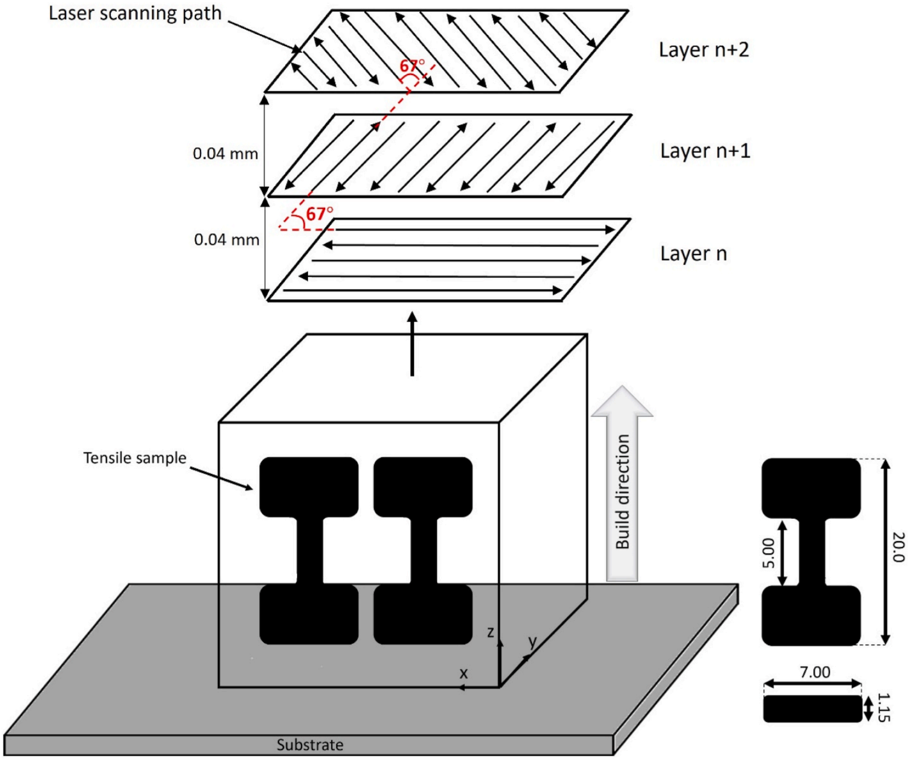

**Fig. 1.** Schematic of the mini tensile test samples orientation machined from the printed blocks, depicting build direction orientation, laser scanning path, and tensile sample dimensions.

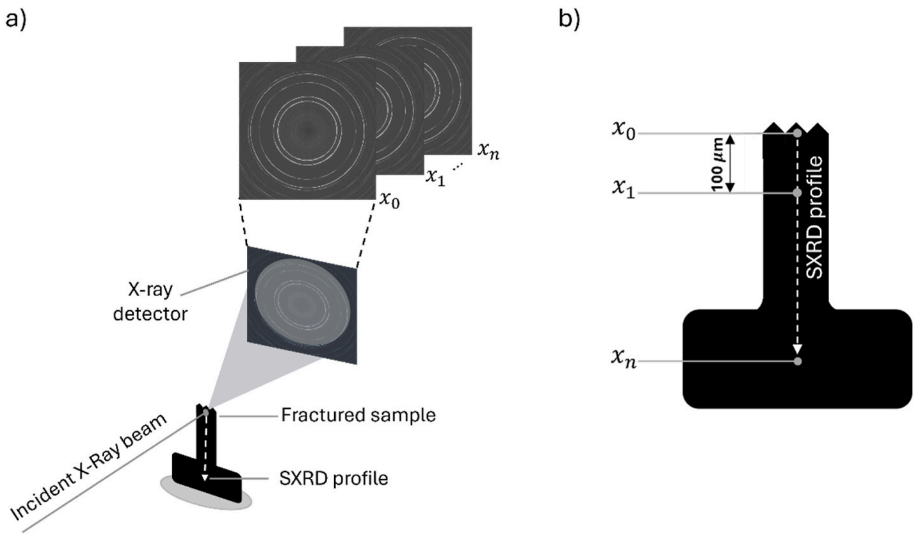

**Fig. 2.** SXRD setup applied to the samples showing a schematic of the: a) beamline setup and b) line scanning profile path through the fractured samples.

(0.1423 Å), was used. A PerkinElmer detector was used to acquire the 2D Debye-Scherrer diffraction ring images. $LaB_6$ powder was used for calibration. The setup of the experiment is presented in Fig. 2, where a step size line profile of 100 µm was used. The raw data was processed using the open-source software Pydidas [24] and in-house developed Python routines. The Debye-Scherrer rings were integrated over 360° to create 1-D diffraction patterns, further refined with Pydidas software. The γ-f.c.c. and ε-h.c.p. volume fractions were determined following the methodology described in Ref. [25], where $\{100\}_{\varepsilon}$, $\{101\}_{\varepsilon}$, $\{102\}_{\varepsilon}$, $\{103\}_{\varepsilon}$, and $\{202\}_{\varepsilon}$ family planes were used for ε-h.c.p. phase, while $\{111\}_{\gamma}$, $\{200\}_{\gamma}$, and $\{222\}_{\gamma}$ family planes were used for γ-f.c.c.

The lattice parameters $a_{\gamma\text{-f.c.c.}}$, $a_{\varepsilon\text{-h.c.p.}}$, and $c_{\varepsilon\text{-h.c.p.}}$ were calculated based on Bragg's law and the interplanar spacing for FCC and HCP crystal structure. The $(c/a)_{\varepsilon\text{-h.c.p}}$ ratio was calculated based on the family planes {100}ε and {102}ε.

## 3. Results

While the primary focus of this study pertains to phase transformation and phase stability, it is important to address the quality of the printed samples. The fabricated specimens exhibited minimal defects, including porosity, lack of fusion, or hot cracks. However, adding $B_4C$ resulted in samples with reduced density and a higher incidence of defects than those produced without $B_4C$. Fig. S2 in the Supplementary Material presents detailed information on the defects observed in the fabricated samples, shown through representative micrographs of the polished sample surfaces.

### 3.1. *Microstructural characterization*

Fig. 3 depicts the SXRD patterns for as-printed samples. The intensity is shown on a logarithmic scale to improve the visualization of low-intensity peaks. The same line colors correspond to the same process parameters, besides sample names are depicted on the right side. Notably, alongside the γ-f.c.c. peaks, the presence of ε-h.c.p., and an intermetallic compound of Cr and Si are discernible for both alloys. Furthermore, a low-intensity σ phase was observed. Note that through the diffraction spectra observed in Fig. 3, no new phases were formed due to $B_4C$ addition. Table 3 depicts the lattice parameters of the γ-f.c.c. and ε-h.c.p. phases. The γ-f.c.c. lattice parameters of BC and CS are similar, while the $(c/a)_{\varepsilon\text{-h.c.p.}}$ ratios for BC alloys are higher than for CS. Note that $(c/a)_{\varepsilon\text{-h.c.p.}}$ values for CS and BC are significantly lower than the ideal value (≈ 1.633).

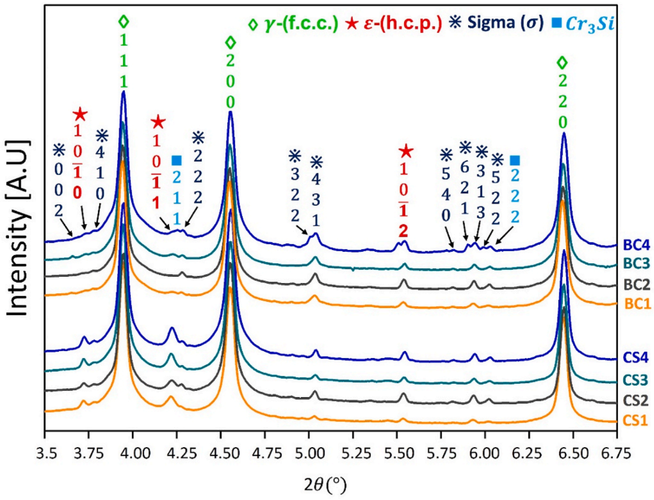

**Fig. 3.** SXRD pattern of the bulk samples as-printed for all conditions. The same line colors correspond to the same process parameters. (For interpretation of the references to color in this figure legend, the reader is referred to the Web version of this article.)

**Table 3**
Lattice parameters of the γ-f.c.c. and ε-h.c.p. phases for both CS and BC alloys.

| Sample n° | Phase | | | | c/a ratio |
|---|---|---|---|---|---|
| | Specimen | γ-f.c.c. | ε-h.c.p. | | |
| | | $a_{\gamma(f.c.c)}$ (Å) | $a_{\varepsilon(h.c.p)}$ (Å) | $c_{\varepsilon(h.c.p)}$ (Å) | |
| 1 | CS | 3.582 | 2.532 | 4.084 | 1.613 |
| | BC | 3.583 | 2.529 | 4.107 | 1.624 |
| 2 | CS | 3.581 | 2.530 | 4.086 | 1.615 |
| | BC | 3.580 | 2.528 | 4.100 | 1.622 |
| 3 | CS | 3.581 | 2.531 | 4.086 | 1.615 |
| | BC | 3.580 | 2.527 | 4.102 | 1.624 |
| 4 | CS | 3.579 | 2.529 | 4.088 | 1.616 |
| | BC | 3.578 | 2.526 | 4.101 | 1.624 |

Fig. 4 shows a combination of phase map and image quality map for CS (first column) and BC alloys (second column). The amount of γ-f.c.c. and ε-h.c.p. phases are depicted on the right upper corner of each map. While CS samples present a large amount of ε-h.c.p., achieving values between 60.1 and 81.4 %, BC samples present almost no presence of this phase. The CS2 and CS4 alloys (Fig. 4c and g) present ε-h.c.p. in columnar morphology, as large grains. Furthermore, CS1 (Fig. 4a) presents the highest amount of ε-h.c.p., while CS3 (Fig. 4e) presents the lowest value among alloys without $B_4C$. Regarding alloys with $B_4C$, although BC3 (Fig. 4f) presents almost no ε-h.c.p., the amount of this phase detected for other BC conditions was also very low, achieving a maximum of 3.7 % (Fig. 4d).

Owing to ε-h.c.p. formation, the grain size and morphology analysis of prior γ-f.c.c. is compromised by conditions that present significant transformation volume, as γ-f.c.c. fragmentation occurs with its decomposition in ε-h.c.p. Therefore, prior γ-f.c.c. crystallographic orientation was calculated for CS conditions to better analyze these parameters, while simple γ-f.c.c. orientation (as measured) is shown for BC alloys. These results are depicted in Fig. 5. White points on CS results refer to non-indexed, low index quality, and lack of Shoji-Nishiyama (S-N) orientation relationship (OR) correspondence.

It is noted that CS alloys present elongated γ-f.c.c. grains aligned with the build direction, as well as larger grains when compared to BC samples. The grain morphology of these samples also seems to depend on the process parameters, as CS2 presents larger and more elongated γ-f.c.c. grains, while the opposite occurs to CS1. Although some CS results present the majority of one specific orientation, for instance, CS4, it is not possible to state that there is an orientation texture, as the regions analyzed by EBSD are small. Regarding BC conditions, these samples present finer and equiaxed grains, although some columnar grains are still visible but smaller than those columnar grains observed for CS samples.

### 3.2. *Mechanical behavior*

Fig. 6 illustrates the tensile engineering stress-plastic strain curves for the as-printed samples, while Table 4 shows the yield strength (YS), elongation to failure (EF), and the ultimate tensile strength (UTS) calculated for each condition. For the CS alloys, despite all the conditions presenting a similar YS, EF, and UTS, CS3 resulted in the highest UTS value (843.0 ± 14.0 MPa), while the highest YS (508.0 ± 9.5 MPa) and EF (25.0 ± 0.1 %) were found for CS1 and CS2, respectively. The results for BC samples are detailed in Fig. 6 insert, where BC2 presented values of YS 497.0 ± 20.0 MPa, while BC1, BC3, and BC4 presented values of approximately 670 MPa. The highest EF was found in BC2, although it was just 5.0 ± 0.1 %.

After tensile tests, SXRD line profiles were performed at one part of the fractured samples (as depicted in the setup presented in Fig. 1). Fig. 7 illustrates a schematic representation of the findings. The observed diffraction rings presented in Fig. 7a correspond to two distinct regions:

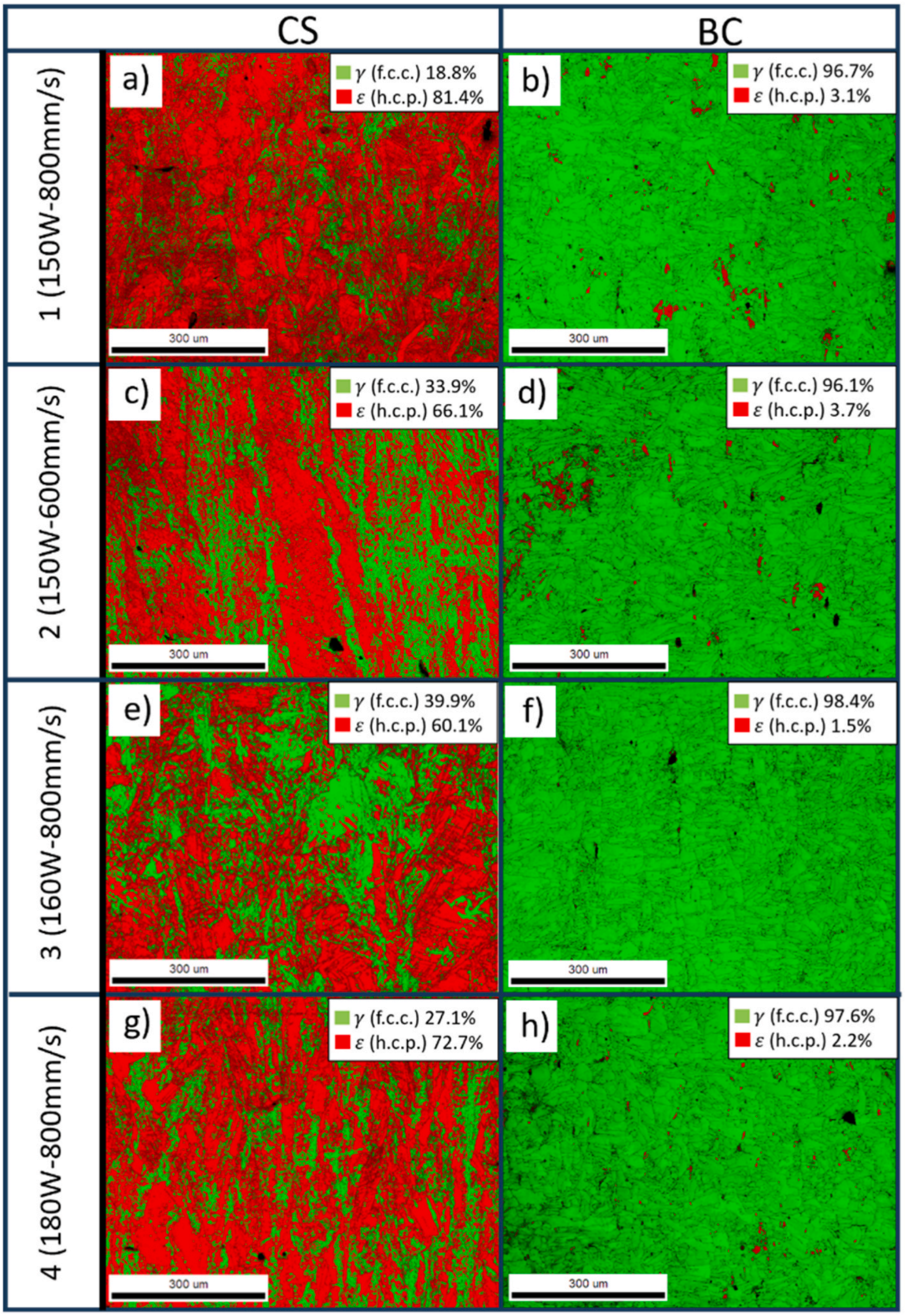

**Fig. 4.** EBSD phase map + image quality map for samples without $B_4C$ (first column) and with 0.25 wt% of $B_4C$ (second column). Rows indicate the parameters used for each condition. The green color indicates the γ-f.c.c. phase, while the red color indicates the ε-h.c.p. phase. (For interpretation of the references to color in this figure legend, the reader is referred to the Web version of this article.)

the bulk, non-deformed area ($X_n$), and the deformed area ($X_0$) for both CS and BC samples. It is important to highlight that these diffraction patterns were obtained under condition 1 (150 W-800 mm/s); however, similar behavior was observed across all experimental conditions. The schematic tensile specimen (Fig. 7b) indicates the regions corresponding to $X_0$ and $X_n$, as well as the spot size used for the SXRD measurements (100 $\mu$m). The intensity plots for the CS and BC samples are shown in Fig. 7c, and depict the phase evolution across the sample, spanning from the fracture zone to the non-deformed region. The diffractograms obtained for the deformed region ($X_0$) display diffraction peaks for both CS and BC as a function of interplanar spacing, as presented in Fig. 7d. Notably, in the CS1 condition, the presence of the ε-h.c.p. phase was evident, indicating the occurrence of the TRIP effect. Conversely, these diffraction peaks were less pronounced under the BC condition.

Building on the results presented in Fig. 7 and the emergence of the ε-h.c.p. phase, further investigation was conducted to assess the extent of phase transformation throughout the specimen following deformation. Fig. 8 illustrates the ε-h.c.p. volume fraction profile from the fracture region toward the non-deformed section, with Fig. 8a providing a detailed view from the ε-h.c.p. volume fraction evolution for CS conditions and Fig. 8b for BC conditions. In the non-deformed regions, the ε-h.c.p. fraction is negligible, increasing progressively towards the fracture across all samples. Similar behavior is observed inside each group of samples (CS or BC conditions); however, a much lower amount of ε-h.c.p. was found close to fracture for BC alloys, achieving $f_\varepsilon$ lower than 0.12 and decreasing from the fracture at a shorter range than CS

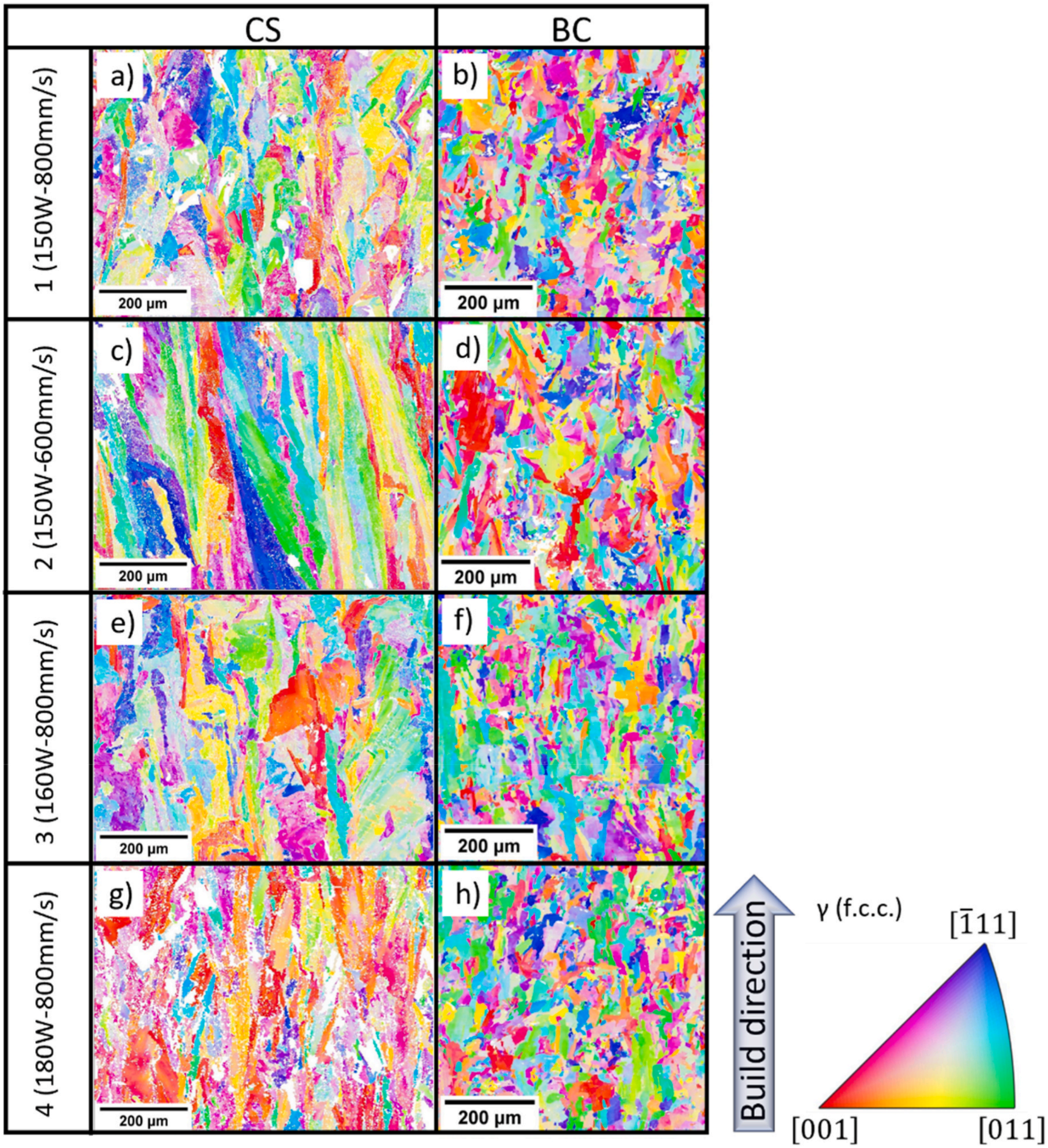

**Fig. 5.** EBSD inverse pole figure map for: (i) first column (CS alloys) – prior γ-f.c.c. orientation calculated following the Shoji-Nishiyama orientation relationship, and (ii) second column (BC alloys) – measured γ-f.c.c. orientation. White points refer to either non-indexed, ε-h.c.p. (in BC samples), and regions with differences from the S-N relationship above the established criteria (in CS samples).

samples. For these later, however, $f_\varepsilon$ reaches values between 0.60 and 0.70 near the fracture and decreases gradually until ≈3.5 mm from the fracture, when it begins to decrease more rapidly. Low-intensity peaks of precipitates, such as σ-phase, were not considered on these ε-h.c.p. volume fraction evolution, the calculations being regarded to only ε-h.c.p. and γ-f.c.c. phases.

## 4. Discussion

### *4.1. Effects of power and scanning speed on the microstructural evolution*

The CS samples exhibited a strong dependence of grain morphology on process parameters, unlike BC samples. CS1 shows well-defined melt pools, whereas CS2 displays only a columnar structure (Fig. 5). These differences could be attributed to variations in cooling rates. Tan et al. [26] highlighted that LPBF parameters influence molten pool dynamics, solidification, and grain structure, with factors like scanning speed affecting the balance between columnar and equiaxed grains. Similarly, Agrawal et al. [9] demonstrated grain morphology changes by adjusting LPBF parameters, via Equation (2) [27].

$$R = V\cos\theta \tag{2}$$

where θ is the angle between growth and scanning direction. The cooling rate, expressed as *GR* (where G is the thermal gradient) [28], increases with increasing scanning speeds, as R increases with V. It promotes finer grain morphology, which explains the observed differences in CS samples.

The BC alloys displayed a refined structure with a lower aspect ratio than CS alloys (Fig. 5), but without significant variation. Adding $B_4C$

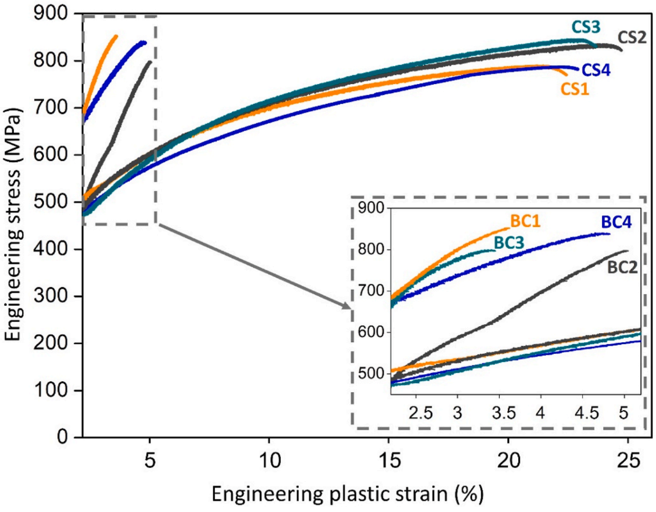

**Fig. 6.** Engineering plastic strain vs engineering stress curve for as-printed samples. The inserted figure depicts conditions that presented low elongation (BC alloys).

**Table 4**
Mechanical behavior of as-printed a) CS and b) BC samples.

| Sample nº | Specimen | YS (MPa) | EF (%) | UTS (MPa) |
|---|---|---|---|---|
| 1 | CS | 508.0 ± 9.5 | 22.0 ± 0.01 | 789.0 ± 17.5 |
| | BC | 670.0 ± 7.5 | 3.60 ± 0.03 | 854.0 ± 24.0 |
| 2 | CS | 489.0 ± 13.5 | 25.00 ± 0.11 | 833.0 ± 13.3 |
| | BC | 497.0 ± 20.0 | 5.00 ± 0.01 | 800.0 ± 10.5 |
| 3 | CS | 479.0 ± 23.0 | 24.00 ± 0.10 | 843.0 ± 14.0 |
| | BC | 665.0 ± 10.0 | 3.50 ± 0.01 | 800.0 ± 49.0 |
| 4 | CS | 471.0 ± 12.5 | 23.00 ± 1.75 | 785.0 ± 18.5 |
| | BC | 665.0 ± 52.5 | 4.80 ± 0.01 | 840.0 ± 101.0 |

enhanced the melt pool thermal stability during LPBF processing, stabilizing solidification dynamics despite parameter fluctuations. This promoted a uniform microstructure across varied conditions, reducing sensitivity to changes in *P* and *V*. As shown in Table 4, increasing *V* while keeping *P* constant reduces both YS and UTS, as seen in the comparison of CS1 and CS2. In contrast, increasing *P* at a constant *V* raises UTS, as observed in CS1 versus CS4. The increase in *V* from 600 mm/s (CS2) to 800 mm/s (CS1) lowers the linear energy density, reducing energy input per unit length and causing insufficient local powder melting. Chen et al. [29] linked this insufficient melting to non-uniform solidification and defect formation. Additionally, Tan et al. [30] reported that higher scanning speeds lead to inadequate fusion and weak interlayer bonding, negatively impacting mechanical performance. These factors collectively explain the observed reductions in YS, UTS, and ductility.

In summary, increasing *V* seems to change the grain morphology from columnar to equiaxial grains and decrease the solidification defects, leading to higher mechanical properties for CS samples. On the other hand, adding $B_4C$ refines the grain size and induces its morphology to equiaxed grains, as evidenced by EBSD analysis (Fig. 5). This suggests that $B_4C$ may serve as a heterogeneous nucleation agent during solidification, enhancing microstructural uniformity. However, despite the refined and equiaxed structure, BC samples exhibited lower mechanical performance, which will be discussed in the following sections.

### 4.2. *Influence of $B_4C$ on the ε-h.c.p. presence for printed parts*

Regarding the ε-h.c.p. presence, two main questions arise: (i) the higher amount of phase transformation during the tensile test of CS samples and (ii) the difference in ε-h.c.p. volume fraction observed via SXRD and EBSD techniques.

Olson and Cohen [31] showed that γ-f.c.c. → ε-h.c.p. phase transformation is governed by the Gibbs free energy change for ε-h.c.p. formation ($\Delta G_{\gamma\rightarrow\varepsilon}$) from the γ-f.c.c. phase. Additionally, literature has shown that greater γ-f.c.c. phase stability results in a lower driving force for the TRIP effect due to a corresponding higher $\Delta G\gamma\rightarrow\varepsilon$ [32–34]. Additionally, lower $\Delta G\gamma\rightarrow\varepsilon$ values indicate reduced stacking fault energy (SFE) in the system, as ε-h.c.p. formation relies on the presence of stable intrinsic stacking faults within the microstructure. Therefore, increased γ-f.c.c. phase stability is effectively associated with an increase in the SFE of the system [6]. Both $\Delta G\gamma\rightarrow\varepsilon$ and SFE are related in Equation (3) [32–34].

$$\mathrm{SFE} = 2\rho\left(\Delta G^{\gamma\rightarrow\varepsilon} + \Delta G_{\mathrm{ex}}\right) + 2\sigma^{\gamma/\varepsilon} \tag{3}$$

where ρ is the molar surface density for the $\{111\}\gamma$ closed packed planes (mol/m$^2$) and $\sigma^{\gamma/\varepsilon}$ is the energy per surface unit of the {111} interface between the γ and ε phase boundary (J/m$^2$) [31]. $\Delta G_{ex}$ is the excess energy inversely proportional to the grain size and can be calculated according to Ref. [35].

The stability of the γ-f.c.c. phase in BC alloys is intricately linked to SFE, which is influenced by both microstructural features and elemental distribution. The presence of stacking faults facilitates the nucleation of the ε-h.c.p. phase by the introduction of stacking faults via the sweeping of partial dislocations around a pole dislocation or through the overlapping of stacking faults [36]. However, as reported by Thapliyal et al. [14], the retention of carbon in solid solution, particularly under the rapid solidification conditions of LPBF, leads to an increase in SFE, potentially suppressing the deformation-induced γ-f.c.c.→ε-h.c.p. transformation. This is because carbon is readily accommodated within the interstitial γ-f.c.c lattice sites due to its small atomic radius, whereas boron tends to segregate to cell boundaries as it cannot be stably incorporated in either interstitial or substitutional positions [37]. Some authors have shown, through thermodynamic and empirical equations, the influence of carbon and other elements on the SFE [38,39], corroborating the present conclusion. Additionally, the $B_4C$ alloying decreased the grain size and, according to Saeed-Akbari et al. [35], it increases the SFE, consequently increasing γ-f.c.c. stability. Therefore, the higher carbon content and lower prior γ-f.c.c. grain size increase γ-f.c.c. stability by increasing the energy barrier for the TRIP effect.

The discrepancy in ε-h.c.p. phase fraction observed between EBSD and SXRD analyses in our CS samples highlights the critical influence of surface effects on *γ*-f.c.c. stability. While EBSD offers valuable surface-sensitive microstructural insights, it is inherently limited by its surface localization. As demonstrated by Lomholt et al. [40] studying TRIP steels, *γ*-f.c.c. grains are mechanically stabilized within the bulk, a condition disrupted by the metallographic preparation required for EBSD. Creating a free surface removes the normal stress constraint, leading to stress relaxation that can significantly affect the stability and transformation kinetics of near-surface *γ*-f.c.c., potentially misrepresenting the bulk behavior. Our observation of a higher ε-h.c.p. phase fraction at the surface directly reflects this stress-induced instability of *γ*-f.c.c. phase.

In contrast, our SXRD measurements, conducted in transmission mode, yielded data from a larger, stress-unaffected volume of the material, providing a more accurate assessment of the bulk phase stability and transformation behavior. This bulk-sensitive approach avoids the artifacts introduced by surface preparation and stress relaxation, offering a more representative picture of the intrinsic material response. This is consistent with the findings of Tirumalasetty et al. [41], who, using combined EBSD and XRD, demonstrated a greater propensity for surface *γ*-f.c.c. to transform compared to its bulk counterpart in TRIP 800 steel.

The increased ε-h.c.p. fraction we observe on the surface is thus a direct consequence of the altered stress state and the inherent instability of *γ*-f.c.c. at the surface, exacerbated by metallographic preparation. This further emphasizes the need for bulk-sensitive characterization techniques to accurately capture phase stability and transformation

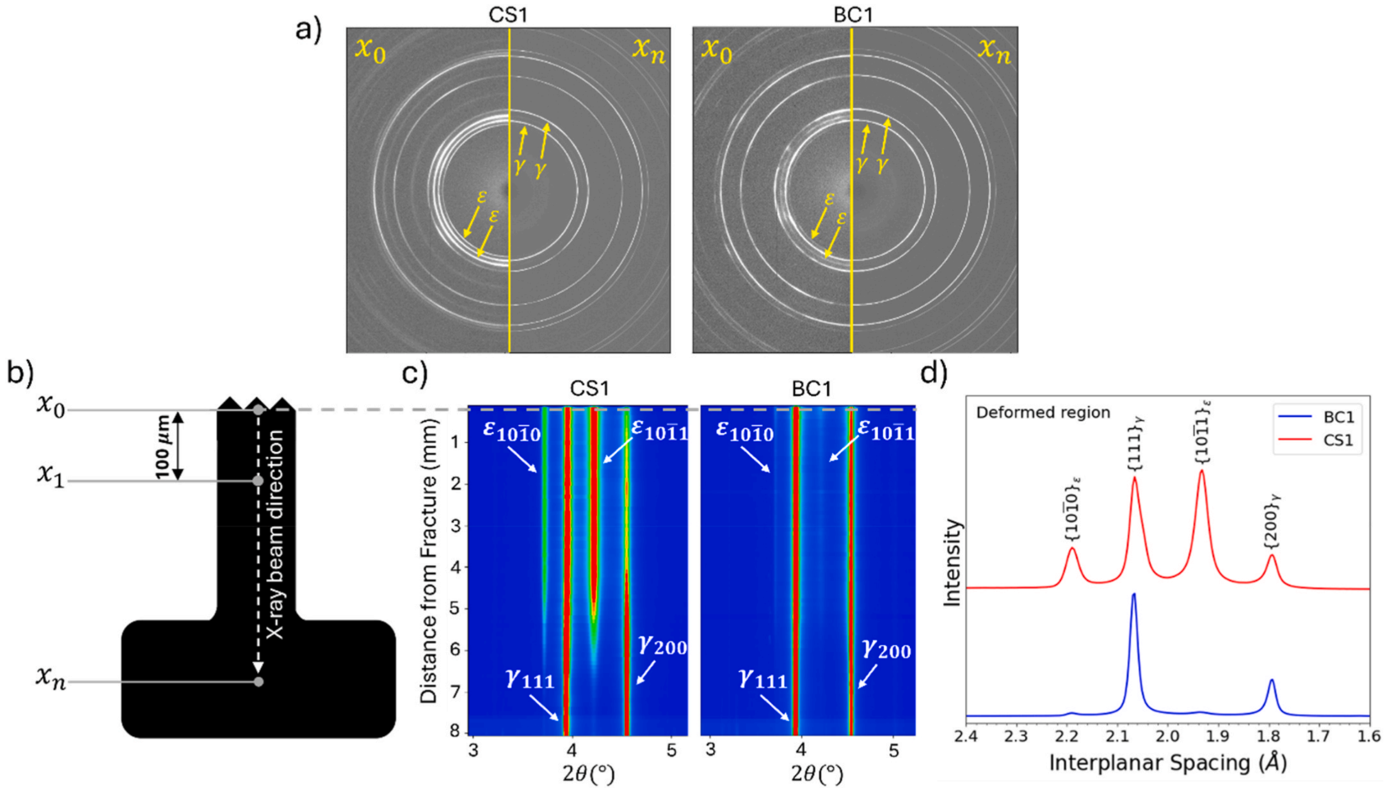

**Fig. 7.** Schematic representation of the SXRD line profile conducted on the CS and BC samples, illustrating: a) diffraction rings for both deformed and non-deformed regions, b) tensile specimen after deformation, c) diffraction intensity maps, and d) diffractogram at the deformed region highlighting the TRIP effect.

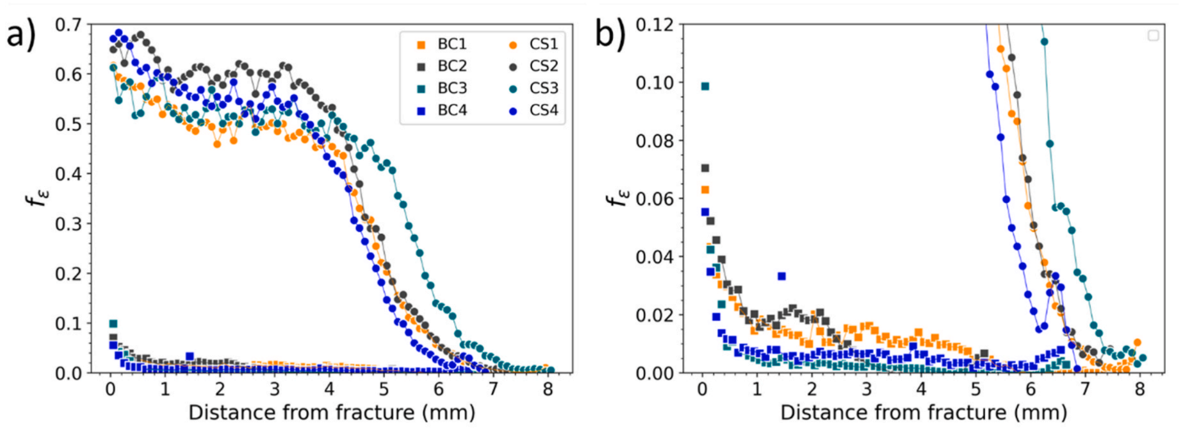

**Fig. 8.** a) ε-h.c.p. volume fraction evolution of tensile fractured samples from fracture towards non-deformed material for both CS and BC alloys. b) Detail of $f_\varepsilon$ evolution for BC samples.

mechanisms, especially when investigating materials where surface effects may play a significant role.

### 4.3. Phase stability during tensile loading

Both alloys exhibit a predominantly γ-f.c.c. dual-phase microstructure in the as-printed condition (Fig. 3). The ε-h.c.p. phase fraction was minimal, not exceeding 2 % in BC alloys and 1 % in CS alloys. A small amount of σ-phase was also present in both systems. However, after tensile testing, line-scan SXRD on fractured test specimens (Fig. 2b), revealed a greater volume fraction of ε-h.c.p. phase for CS samples compared to the BC samples.

In the region of highest strain near the fracture tip, CS alloys exhibited a substantial increase in the ε-h.c.p. phase fraction, rising from 1 vol % to between 60 and 70 vol %, at the expense of a decrease in the γ-f.c.c. phase. This indicates an activation of the TRIP effect for these alloys. Conversely, for BC alloys, the ε-h.c.p. phase fraction increased from 2 vol % to between 6 and 12 vol %. The same discussion regarding the higher γ-f.c.c. stability due to higher carbon content and lower grain size can be applied for the larger amount of ε-h.c.p. for CS samples, where these factors render the ε-h.c.p. transformation notably more evident. However, another factor arises: the amount of deformation. While the CS samples passed 20 % of EF, the highest value obtained for BC samples was 5 %. Thapliyal et al. [14] studying the same base material but with 0.5 wt % of $B_4C$ addition found that carbon and boron segregate on grain and cell boundaries. The authors also found that little

TRIP effect was found for as-printed $B_4C$ added alloys, while further annealing improved their ductility and increased the amount of TRIP effect observed.

Gao et al. [42] suggested that boron positively changes the mechanical properties by changing the grain boundary properties, thus improving both tensile strength and plasticity. Besides, Kolb et al. [43] say that an addition of a high amount of B could lead to mechanical properties degradation due to phase transformation phenomena in the grain boundary. Ahn et al. [44] reported a much higher YS when adding $B_4C$ to the alloy, being justified mainly due to the high dislocation density promoted by the precipitates. While the authors reported a substantial decrease in elongation, they did not address the possible reasons for it. Finally, the present authors are willing that a higher amount of defect found for as-printed alloys could lead to their premature failure, avoiding the further γ-f.c.c.→ε-h.c.p. phase transformation. However, although BC samples presented a higher fraction of defects, the difference is not enough to lead to such a strong decrease in the mechanical properties, as seen in the Supplementary material (Fig. S1 and Table S1). Moreover, the EBSD results of as-printed samples confirmed that BC samples present higher γ-f.c.c. stability, as even with surface stress relief and metallographic preparation, it was not observed a large amount of ε-h.c.p. phase as found for the CS conditions.

Therefore, considering the differences in the chemical composition of CS and BC samples, as well as the resulting ductility and the TRIP effect observed during the tensile test, it is reasonable to conclude that the TRIP effect was not entirely suppressed. However, the addition of $B_4C$ particles led to a marked reduction in elongation at break, indicating premature material failure and a decrease in ductility, potentially hindering the full manifestation of the TRIP effect. This suggests that, although the $B_4C$ addition may enhance strength, it compromises the overall mechanical performance due to increased brittleness. It is important to note that an increase in SFE due to alloying [38] or grain size refinement [45] does not necessarily reduce plasticity, and indeed can even promote twinning-induced plasticity (TWIP) effect within a specific SFE range (15–45 $mJ/m^2$) [46,47], which is well-documented to enhance plasticity [48,49].

### 4.4. Influence of $B_4C$ alloying on ε-h.c.p. deformation

It is well established that the c/a ratio is closely linked to the lattice strain associated with the ε-h.c.p. phase and the activation of distinct slip systems [50,51]. When the c/a ratio exceeds the ideal value of 1.633, basal plane slip primarily governs the plastic deformation process. Conversely, if the c/a ratio is less than the ideal 1.633 value, the pyramidal slipping becomes dominant. Additionally, c/a ratios below the ideal value promote the development of twinning as a deformation mechanism [52].

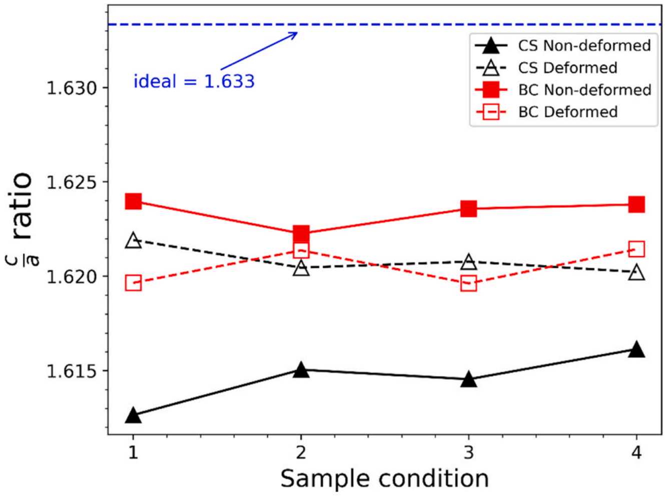

**Fig. 9.** c/a ratio as a function of samples processing condition for CS and BC alloys, before and after deformation.

The c/a ratios for ε-h.c.p. in both CS and BC alloys before and after deformation are presented in Fig. 9. The increase in the c/a ratio with strain in CS alloys can be attributed to an elongation along the *c*-axis accompanied by a slight contraction along the *a*-axis. Conversely, BC samples exhibit the opposite behavior, characterized by a contraction along the *c*-axis and a slight extension along the *a*-axis, as detailed in the Supplementary material (Table S2). The c/a ratio at all strain levels remains below the ideal value, which, according to Haridas et al. [53], indicates the capacity of the material to accommodate strain during high deformation through the activation of non-basal slip modes.

Initially, the microstructure of CS alloys exhibited a high fraction of the γ-f.c.c. phase, as evident from the SXRD pattern in Fig. 3 and the non-deformed region in the fractured tensile test sample shown in Fig. 8. Substantial phase transformation occurred following tensile deformation, resulting in 60–70 vol% of the ε-h.c.p. phase. This indicates that most of the ε-h.c.p. phase was formed during deformation, rather than being retained from the original as-printed structure. Accordingly, the c/a ratio of the newly formed ε-h.c.p., as described by Sinha et al. [7], reflects its intrinsic electronic configuration and elastic deformation characteristics, representing its fundamental lattice properties rather than strain-induced modifications.

For BC alloys, the initial c/a ratio was higher than those found for CS alloys, consistent with the findings of Bhowmik et al. [54], who reported that the c/a ratio varies with chemical composition. Stanford and Dunne [55] reported that for the Fe-Mn-Si alloy system, adding ε-h.c.p. phase stabilizers increases the lattice distortion and raises the c/a ratio. Conversely, adding γ-f.c.c. phase stabilizers, such as C, promote a decrease in the c/a ratio [54], the opposite of what was observed in the present work. This contradiction can be attributed to the dominant role of boron in $B_4C$. With its small atomic radius (≈85 pm), boron induces anisotropic lattice distortions, stabilizing the ε-h.c.p. phase and increasing the c/a ratio. Although C is generally regarded as a γ-f.c.c. stabilizer, the distortion effects introduced by boron outweigh the influence of carbon in this specific system, explaining the observed c/a ratio increase. Shen et al. [52] conducted in situ SXRD analysis on a metastable $Fe_{42}Mn_{28}Co_{10}Cr_{15}Si_5$ alloy during tensile testing at a constant strain rate and reported a slight decrease in the *c*-axis of 0.36 % and an expansion of 0.69 % on the *a*-axis, resulting in a reduction in the c/a ratio of ≈1 %. This phenomenon leads to the activation of pyramidal slip systems and deformation twinning, which, according to Frank et al. [51], can accommodate deformation along the *c*-axis at high strain levels.

In summary, the alloys exhibited distinct effects on the c/a ratio post-deformation: CS alloys showed an increase in the c/a ratio, while BC alloys exhibited a decrease. The observed changes in lattice behavior — *c*-axis contraction and *a*-axis expansion in BC alloys, compared to the opposite trend in CS alloys—demonstrate that the addition of $B_4C$ significantly alters the deformation-induced transformation mechanisms, particularly the TRIP effect. These changes likely stem from the influence of $B_4C$ on the γ-f.c.c. → ε-h.c.p. transformation pathway, affecting strain accommodation and consequently modifying the mechanical properties.

The variation in the TRIP response highlights the complex role of $B_4C$ in phase stability and its potential to influence deformation behavior under different loading conditions. Moreover, a comprehensive understanding of the influence of $B_4C$, particularly its effect on the c/a ratio, material properties, and phase behavior, is crucial. Further investigations are required to evaluate its impact on phase transformation kinetics, optimize its content for phase stability, and quantitatively assess its effects on the TRIP effect. By strategically manipulating nanoparticle additions to modulate the c/a ratio, we can effectively optimize phase stability, the deformation mechanisms, and ultimately engineer advanced materials with enhanced strength, ductility, and resistance to failure for a wide spectrum of applications.

## 5. Conclusions

This study investigates the influence of $B_4C$ alloying on the phase transformation of metastable HEAs fabricated via LPBF. Key findings from the analysis of microstructural and mechanical properties of samples with (BC alloys) and without $B_4C$ (CS alloys), influenced by varying process parameters, are as follows:

1. The CS alloys exhibited a strong sensitivity to variations in laser power and scanning speed, resulting in significant microstructural differences in grain size and morphology across the various printing conditions. Conversely, these factors remained relatively stable for BC alloys under similar processing variations. It suggests that the grain growth mechanism in CS alloys is more susceptible to processing parameter changes than in BC alloys.
2. Incorporating $B_4C$ reduced the grain size, which increased the stacking fault energy, thereby enhancing the stability of the γ-f.c.c. phase.
3. Under all tested conditions, the CS alloys exhibited similar values of yield strength, ultimate tensile strength, and elongation to failure. The incorporation of $B_4C$ led to a significant increase in yield strength, attributed to solid solution and particle strengthening mechanisms within the HEA composition. However, it did not lead to a substantial enhancement of the ultimate tensile strength. CS alloys demonstrated a pronounced TRIP effect, as evidenced by their increased elongation, whereas the BC alloys did not exhibit this behavior. The addition of $B_4C$ may have contributed to premature failure, as indicated by the reduced ductility, potentially preventing the complete manifestation of the TRIP effect.
4. Both CS and BC alloys exhibited a c/a ratio smaller than the ideal value of 1.633. The increase in the c/a ratio with strain in the CS alloys is attributed to elongation along the *c*-axis, accompanied by a slight contraction along the *a*-axis. In contrast, the BC samples displayed the opposite behavior, with contraction along the *c*-axis and slight extension along the *a*-axis, resulting in a decrease in the c/a ratio. Considering the predominantly γ-f.c.c. microstructure of the CS alloys, the substantial phase transformation observed suggests that the majority of the ε-h.c.p. phase was formed during deformation, rather than being retained from the initial as-printed structure.
5. Our findings reveal a significant divergence in ε-h.c.p. phase fraction between surface-sensitive (EBSD) and bulk-sensitive (SXRD) analyses, emphasizing the inherent instability of γ-f.c.c. at free surfaces. Metallographic preparation-induced stress relaxation profoundly impacts near-surface phase stability, requiring bulk-sensitive techniques to accurately elucidate true material response and avoid misinterpretations in stress-mediated phase transformation studies.

These findings highlight the significant impact of the influence of $B_4C$ addition on the microstructural evolution and mechanical performance of additively manufactured HEAs, playing a key role in improving the microstructural quality and performance of HEAs and offering new possibilities for advanced manufacturing applications.

## CRediT authorship contribution statement

**I.A.B. Moura:** Writing – review & editing, Writing – original draft, Visualization, Validation, Methodology, Investigation, Formal analysis, Data curation, Conceptualization. **G.G. Ribamar:** Writing – review & editing, Visualization, Validation, Software, Investigation, Formal analysis, Data curation. **P. Agrawal:** Visualization, Validation, Investigation, Data curation. **A. Roy:** Visualization, Validation, Methodology, Investigation, Data curation. **J. Shen:** Writing – review & editing, Visualization, Validation, Investigation. **P. Freitas Rodrigues:** Writing – review & editing, Visualization, Validation. **E. Maawad:** Writing – review & editing, Visualization, Validation, Resources. **N. Schell:** Writing – review & editing, Visualization, Validation, Resources. **A.B. Pereira:** Writing – review & editing, Visualization, Validation. **J.P. Oliveira:** Writing – review & editing, Visualization, Validation, Supervision, Resources, Project administration, Methodology, Investigation, Funding acquisition, Conceptualization. **R.S. Mishra:** Visualization, Validation, Supervision, Resources, Project administration, Methodology, Investigation, Funding acquisition, Conceptualization.

## Declaration of competing interest

The authors declare that they have no known competing financial interests or personal relationships that could have appeared to influence the work reported in this paper.

## Acknowledgments

The authors acknowledge the infrastructure and support of the Center for Agile & Adaptive and Additive Manufacturing (CAAAM) funded through State of Texas Appropriation #190405-105-805008-220. The authors thank the Materials Research Facility for access to microscopy facilities at the University of North Texas. I. A. B. Moura acknowledges Fundação para a Ciência e Tecnologia (FCT – MCTES) for funding the PhD grant (2021.08034.BD). JS and JPO acknowledge the funding by national funds from FCT - Fundação para a Ciência e a Tecnologia, I.P., in the scope of the project's LA/P/0037/2020, UIDP/50025/2020 and UIDB/50025/2020 of the Associate Laboratory Institute of Nanostructures, Nanomodelling and Nanofabrication – i3N. P.F. R. acknowledges funding by FCT – Fundação para a Ciência e a Tecnologia, under projects UID/00285 - Centre for Mechanical Engineering, Materials and Processes, LA/P/0112/2020 and CAPES - Novação - 99999.011943/2013-00. The authors acknowledge DESY (Hamburg, Germany), a member of the Helmholtz Association HGF, for providing the experimental facilities. Parts of this research were carried out at the Hereon P07 (HEMS) beamline. The present study was developed in the scope of the Project "Agenda ILLIANCE" [C644919832-00000035 | Project nº 46], financed by PRR – Plano de Recuperação e Resiliência under the Next Generation EU from the European Union.

## Appendix A. Supplementary data

Supplementary data to this article can be found online at https://doi.org/10.1016/j.msea.2025.148607.

## Data availability

Data will be made available on request.

## References

[1] X. Wang, R.R. De Vecchis, C. Li, H. Zhang, X. Hu, S. Sridar, Y. Wang, W. Chen, W. Xiong, Design metastability in high-entropy alloys by tailoring unstable fault energies, Sci. Adv. 8 (2022), https://doi.org/10.1126/sciadv.abo7333.

[2] Z. Pei, S. Zhao, M. Detrois, P.D. Jablonski, J.A. Hawk, D.E. Alman, M. Asta, A. M. Minor, M.C. Gao, Theory-guided design of high-entropy alloys with enhanced strength-ductility synergy, Nat. Commun. 14 (2023) 2519, https://doi.org/10.1038/s41467-023-38111-6.

[3] Z. Li, K.G. Pradeep, Y. Deng, D. Raabe, C.C. Tasan, Metastable high-entropy dual-phase alloys overcome the strength–ductility trade-off, Nature 534 (2016) 227–230, https://doi.org/10.1038/nature17981.

[4] R. Sabban, K. Dash, S. Suwas, B.S. Murty, Strength–ductility synergy in high entropy alloys by tuning the thermo-mechanical process parameters: a comprehensive review, J. Indian Inst. Sci. 102 (2022) 91–116, https://doi.org/10.1007/s41745-022-00299-9.

[5] S.S. Nene, K. Liu, M. Frank, R.S. Mishra, R.E. Brennan, K.C. Cho, Z. Li, D. Raabe, Enhanced strength and ductility in a friction stir processing engineered dual phase high entropy alloy, Sci. Rep. 7 (2017) 16167, https://doi.org/10.1038/s41598-017-16509-9.

[6] S.S. Nene, M. Frank, K. Liu, R.S. Mishra, B.A. McWilliams, K.C. Cho, Extremely high strength and work hardening ability in a metastable high entropy alloy, Sci. Rep. 8 (2018), https://doi.org/10.1038/s41598-018-28383-0.

[7] S. Sinha, S.S. Nene, M. Frank, K. Liu, P. Agrawal, R.S. Mishra, On the evolving nature of c/a ratio in a hexagonal close-packed epsilon martensite phase in transformative high entropy alloys, Sci. Rep. 9 (2019), https://doi.org/10.1038/s41598-019-49904-5.

[8] P. Agrawal, R.S. Haridas, S. Thapliyal, S. Yadav, R.S. Mishra, B.A. McWilliams, K. C. Cho, Metastable high entropy alloys: an excellent defect tolerant material for additive manufacturing, Mater. Sci. Eng., A 826 (2021) 142005, https://doi.org/10.1016/j.msea.2021.142005.

[9] P. Agrawal, S. Thapliyal, P. Agrawal, A. Dhal, R.S. Haridas, S. Gupta, R.S. Mishra, Additive manufacturing of a metastable high entropy alloy: metastability engineered microstructural control via process variable driven elemental segregation, Mater. Sci. Eng., A 872 (2023) 144938, https://doi.org/10.1016/j.msea.2023.144938.

[10] H.-H. König, N.H. Pettersson, A. Durga, S. Van Petegem, D. Grolimund, A. C. Chuang, Q. Guo, L. Chen, C. Oikonomou, F. Zhang, G. Lindwall, Solidification modes during additive manufacturing of steel revealed by high-speed X-ray diffraction, Acta Mater. 246 (2023) 118713, https://doi.org/10.1016/j.actamat.2023.118713.

[11] M. Qu, J. Yuan, A. Nabaa, J. Huang, C.A. Chuang, L. Chen, Melting and solidification dynamics during laser melting of reaction-based metal matrix composites uncovered by in-situ synchrotron X-ray diffraction, Acta Mater. 271 (2024) 119875, https://doi.org/10.1016/j.actamat.2024.119875.

[12] D. Jiang, H. Cui, H. Chen, X. Zhao, G. Ma, X. Song, Wear and corrosion properties of B4C-added CoCrNiMo high-entropy alloy coatings with in-situ coherent ceramic, Mater. Des. 210 (2021), https://doi.org/10.1016/j.matdes.2021.110068.

[13] S.Y. Ahn, F. Haftlang, E.S. Kim, S.G. Jeong, J.S. Lee, H.S. Kim, Boost in mechanical strength of additive manufactured CoCrFeMnNi HEA by reinforcement inclusion of B4C nano-particles, J. Alloys Compd. 960 (2023), https://doi.org/10.1016/j.jallcom.2023.170631.

[14] S. Thapliyal, P. Agrawal, P. Agrawal, S.S. Nene, R.S. Mishra, B.A. McWilliams, K. C. Cho, Segregation engineering of grain boundaries of a metastable Fe-Mn-Co-Cr-Si high entropy alloy with laser-powder bed fusion additive manufacturing, Acta Mater. 219 (2021) 117271, https://doi.org/10.1016/j.actamat.2021.117271.

[15] J.B. Seol, J.W. Bae, Z. Li, J. Chan Han, J.G. Kim, D. Raabe, H.S. Kim, Boron doped ultrastrong and ductile high-entropy alloys, Acta Mater. 151 (2018) 366–376, https://doi.org/10.1016/j.actamat.2018.04.004.

[16] E.D. Hondros, M.P. Seah, Segregation to interfaces, Int. Met. Rev. 22 (1977) 262–301, https://doi.org/10.1179/imtr.1977.22.1.262.

[17] X.L. He, Y.Y. Chu, J.J. Jonas, The grain boundary segregation of boron during isothermal holding, Acta Metall. 37 (1989) 2905–2916, https://doi.org/10.1016/0001-6160(89)90325-8.

[18] D. Raabe, S. Sandlöbes, J. Millán, D. Ponge, H. Assadi, M. Herbig, P.-P. Choi, Segregation engineering enables nanoscale martensite to austenite phase transformation at grain boundaries: a pathway to ductile martensite, Acta Mater. 61 (2013) 6132–6152, https://doi.org/10.1016/j.actamat.2013.06.055.

[19] M.A.V. Chapman, R.G. Faulkner, Computer modelling of grain boundary segregation, Acta Metall. 31 (1983) 677–689, https://doi.org/10.1016/0001-6160(83)90083-4.

[20] R. Wu, A.J. Freeman, G.B. Olson, First principles determination of the effects of phosphorus and boron on iron grain boundary cohesion, Sci. Technol. Humanit. 265 (1994) 376–380, https://doi.org/10.1126/science.265.5170.376, 1979.

[21] E.D. Hondros, Ségrégations intergranulaires.grain boundary segregation the current situation and future requirements, J. Phys. Colloq. 36 (1975), https://doi.org/10.1051/jphyscol:1975413. C4-117-C4-135.

[22] F. Niessen, T. Nyyssönen, A.A. Gazder, R. Hielscher, Parent grain reconstruction from partially or fully transformed microstructures in *MTEX*, J. Appl. Crystallogr. 55 (2022) 180–194, https://doi.org/10.1107/S1600576721011560.

[23] N. Schell, A. King, F. Beckmann, T. Fischer, M. Müller, A. Schreyer, The high energy materials science beamline (HEMS) at PETRA III, Mater. Sci. Forum 772 (2013) 57–61. https://doi.org/10.4028/www.scientific.net/MSF.772.57.

[24] M. Storm, G. Lotze, Pydidas - Python Diffraction Data Analysis Suite (V24.09.19), 2024.

[25] G. Abreu Faria, Exploring Metallic Materials Behavior Through in Situ Crystallographic Studies by Synchrotron Radiation, Universidade Estadual de Campinas, 2014, https://doi.org/10.47749/T/UNICAMP.2014.942993.

[26] Q. Tan, Y. Yin, A. Prasad, G. Li, Q. Zhu, D.H. StJohn, M.-X. Zhang, Demonstrating the roles of solute and nucleant in grain refinement of additively manufactured aluminium alloys, Addit. Manuf. 49 (2022) 102516, https://doi.org/10.1016/j.addma.2021.102516.

[27] R.S. Mishra, S. Thapliyal, Design approaches for printability-performance synergy in Al alloys for laser-powder bed additive manufacturing, Mater. Des. 204 (2021) 109640, https://doi.org/10.1016/j.matdes.2021.109640.

[28] Reza Abbaschian, Lara Abbaschian, Robert E. Reed-Hill, Physical Metallurgy Principles, fourth ed., Cengage Learning, Stamford (USA), 2009.

[29] Z. Chen, Y. Lu, F. Luo, S. Zhang, P. Wei, S. Yao, Y. Wang, Effect of laser scanning speed on the microstructure and mechanical properties of laser-powder-bed-fused K418 nickel-based alloy, Materials 15 (2022) 3045, https://doi.org/10.3390/ma15093045.

[30] C. Tan, X. Zhang, D. Dong, B. Attard, D. Wang, M. Kuang, W. Ma, K. Zhou, In-situ synthesised interlayer enhances bonding strength in additively manufactured multi-material hybrid tooling, Int. J. Mach. Tool Manufact. 155 (2020) 103592, https://doi.org/10.1016/j.ijmachtools.2020.103592.

[31] G.B. Olson, M. Cohen, A mechanism for the strain-induced nucleation of martensitic transformations, J. Less Common. Met. 28 (1972) 107–118, https://doi.org/10.1016/0022-5088(72)90173-7.

[32] B.C. De Cooman, High Mn TWIP steel and medium Mn steel, in: Automotive Steels, Elsevier, 2017, pp. 317–385, https://doi.org/10.1016/B978-0-08-100638-2.00011-0.

[33] L. Rémy, The interaction between slip and twinning systems and the influence of twinning on the mechanical behavior of fcc metals and alloys, Metall. Trans. A 12 (1981) 387–408, https://doi.org/10.1007/BF02648536.

[34] G.G. Ribamar, G. Miyamoto, T. Furuhara, J.D. Escobar, J.A. Ávila, E. Maawad, N. Schell, J.P. Oliveira, H. Goldenstein, On the evolution of austenite during tempering in high-carbon high-silicon bearing steel by high energy X-Ray diffraction, Metall. Mater. Trans. 55 (2024) 93–100, https://doi.org/10.1007/s11661-023-07229-z.

[35] A. Saeed-Akbari, J. Imlau, U. Prahl, W. Bleck, Derivation and variation in composition-dependent stacking fault energy maps based on subregular solution model in high-manganese steels, Metall. Mater. Trans. 40 (2009) 3076–3090, https://doi.org/10.1007/s11661-009-0050-8.

[36] P. Sahu, A.S. Hamada, R.N. Ghosh, L.P. Karjalainen, X-ray diffraction study on cooling-rate-induced $\gamma$fcc → $\varepsilon$hcp martensitic transformation in cast-homogenized Fe-26Mn-0.14C austenitic steel, Metall. Mater. Trans. A Phys. Metall. Mater. Sci. 38 A (2007) 1991–2000, https://doi.org/10.1007/s11661-007-9240-4.

[37] L. Karlsson, H. Nordén, Overview no. 63 non-equilibrium grain boundary segregation of boron in austenitic stainless steel—IV. Precipitation behaviour and distribution of elements at grain boundaries, Acta Metall. 36 (1988) 35–48, https://doi.org/10.1016/0001-6160(88)90026-0.

[38] S. Curtze, V.-T. Kuokkala, A. Oikari, J. Talonen, H. Hänninen, Thermodynamic modeling of the stacking fault energy of austenitic steels, Acta Mater. 59 (2011) 1068–1076, https://doi.org/10.1016/j.actamat.2010.10.037.

[39] G.G. Ribamar, T.C. Andrade, H.C. de Miranda, H.F.G. de Abreu, Thermodynamic stacking fault energy, chemical composition, and microstructure relationship in high-manganese steels, Metall. Mater. Trans. 51 (2020) 4812–4825, https://doi.org/10.1007/s11661-020-05877-z.

[40] T.N. Lomholt, Y. Adachi, A. Bastos, K. Pantleon, M.A.J. Somers, Partial transformation of austenite in Al–Mn–Si TRIP steel upon tensile straining: an *in situ* EBSD study, Mater. Sci. Technol. 29 (2013) 1383–1388, https://doi.org/10.1179/1743284713Y.0000000292.

[41] G.K. Tirumalasetty, M.A. van Huis, C. Kwakernaak, J. Sietsma, W.G. Sloof, H. W. Zandbergen, Deformation-induced austenite grain rotation and transformation in TRIP-assisted steel, Acta Mater. 60 (2012) 1311–1321, https://doi.org/10.1016/j.actamat.2011.11.026.

[42] J. Gao, J. Ma, S. Yang, Z. Guo, J. Ma, H. Li, Z. Jiang, P. Han, Grain boundary co-segregation of B and Ce hindering the precipitates of S31254 super austenitic stainless steel, J. Mater. Res. Technol. 24 (2023) 2653–2667, https://doi.org/10.1016/j.jmrt.2023.03.135.

[43] M. Kolb, L.P. Freund, F. Fischer, I. Povstugar, S.K. Makineni, B. Gault, D. Raabe, J. Müller, E. Spiecker, S. Neumeier, M. Göken, On the grain boundary strengthening effect of boron in $\gamma/\gamma'$ Cobalt-base superalloys, Acta Mater. 145 (2018) 247–254, https://doi.org/10.1016/j.actamat.2017.12.020.

[44] S.Y. Ahn, F. Haftlang, E.S. Kim, S.G. Jeong, J.S. Lee, H.S. Kim, Boost in mechanical strength of additive manufactured CoCrFeMnNi HEA by reinforcement inclusion of B4C nano-particles, J. Alloys Compd. 960 (2023) 170631, https://doi.org/10.1016/j.jallcom.2023.170631.

[45] S.Y. Jo, J. Han, J.-H. Kang, S. Kang, S. Lee, Y.-K. Lee, Relationship between grain size and ductile-to-brittle transition at room temperature in Fe–18Mn–0.6C–1.5Si twinning-induced plasticity steel, J. Alloys Compd. 627 (2015) 374–382, https://doi.org/10.1016/j.jallcom.2014.11.232.

[46] X. Lu, J. Zhao, Z. Wang, B. Gan, J. Zhao, G. Kang, X. Zhang, Crystal plasticity finite element analysis of gradient nanostructured TWIP steel, Int. J. Plast. 130 (2020) 102703, https://doi.org/10.1016/j.ijplas.2020.102703.

[47] S. Lu, Q. Wang, T. Yao, H. Feng, M. Gao, T. Xi, H. Li, L. Tan, K. Yang, Simultaneous improvement of strength and plasticity: Nano-twin construction for a novel high-nitrogen TWIP steel, Int. J. Plast. 183 (2024) 104144, https://doi.org/10.1016/j.ijplas.2024.104144.

[48] X. Feng, X. Liu, S. Bai, Y. Ye, L. Zong, Y. Tang, Mechanical properties and deformation behaviour of TWIP steel at different strain rates, Mater. Sci. Eng., A 879 (2023) 145182, https://doi.org/10.1016/j.msea.2023.145182.

[49] O. Bouaziz, S. Allain, C.P. Scott, P. Cugy, D. Barbier, High manganese austenitic twinning induced plasticity steels: a review of the microstructure properties relationships, Curr. Opin. Solid State Mater. Sci. 15 (2011) 141–168, https://doi.org/10.1016/j.cossms.2011.04.002.

[50] R.S. Mishra, R.S. Haridas, P. Agrawal, High entropy alloys – tunability of deformation mechanisms through integration of compositional and microstructural domains, Mater. Sci. Eng., A 812 (2021) 141085, https://doi.org/10.1016/j.msea.2021.141085.

[51] M. Frank, Y. Chen, S.S. Nene, S. Sinha, K. Liu, K. An, R.S. Mishra, Investigating the deformation mechanisms of a highly metastable high entropy alloy using in-situ neutron diffraction, Mater. Today Commun. 23 (2020) 100858, https://doi.org/10.1016/j.mtcomm.2019.100858.

[52] J. Shen, W. Zhang, J.G. Lopes, Y. Pei, Z. Zeng, E. Maawad, N. Schell, A.C. Baptista, R.S. Mishra, J.P. Oliveira, Evolution of microstructure and deformation mechanisms in a metastable Fe42Mn28Co10Cr15Si5 high entropy alloy: a combined in-situ synchrotron X-ray diffraction and EBSD analysis, Mater. Des. 238 (2024), https://doi.org/10.1016/j.matdes.2024.112662.

[53] R.S. Haridas, P. Agrawal, S. Thapliyal, S. Yadav, R.S. Mishra, B.A. McWilliams, K. C. Cho, Strain rate sensitive microstructural evolution in a TRIP assisted high

entropy alloy: experiments, microstructure and modeling, Mech. Mater. 156 (2021), https://doi.org/10.1016/j.mechmat.2021.103798.

[54] S. Bhowmik, J. Zhang, S.C. Vogel, S.S. Nene, R.S. Mishra, B.A. McWilliams, M. Knezevic, Effects of plasticity-induced martensitic transformation and grain refinement on the evolution of microstructure and mechanical properties of a metastable high entropy alloy, J. Alloys Compd. 891 (2022), https://doi.org/10.1016/j.jallcom.2021.161871.

[55] N. Stanford, D.P. Dunne, Effect of Si on the reversibility of stress-induced martensite in Fe–Mn–Si shape memory alloys, Acta Mater. 58 (2010) 6752–6762, https://doi.org/10.1016/j.actamat.2010.08.041.